Characterization and Correction of Cardiovascular Motion Artifacts in Diffusion-Weighted Imaging of the Pancreas

Ruiqi Geng[1,2], **Yuxin Zhang**[1,2], **Jitka Starekova**[1], **David R Rutkowski**[1,3], **Lloyd Estkowski**[4], **Alejandro Roldán-Alzate**[1,3], **Diego Hernando**[1,2]

[1]Department of Radiology, University of Wisconsin-Madison, Madison, WI, 53705, USA

[2]Department of Medical Physics, University of Wisconsin-Madison, Madison, WI, 53705, USA

[3]Department of Mechanical Engineering, University of Wisconsin-Madison, Madison, WI, 53705, USA

[4]Department of MR, GE Healthcare, Waukesha, WI, 53188, USA

Abstract

Purpose: To assess the effects of cardiovascular-induced motion on conventional diffusion-weighted imaging (DWI) of the pancreas, and to evaluate motion-robust DWI methods in a motion phantom and healthy volunteers.

Methods: 3T DWI was acquired using standard monopolar and motion-compensated gradient waveforms, including in an anatomically accurate pancreas phantom with controllable compressive motion and healthy volunteers (N=8, 10). In volunteers, highly-controlled single-slice DWI using breath-holding and cardiac gating, and whole-pancreas respiratory-triggered DWI were acquired. For each acquisition, the ADC variability across volunteers, as well as ADC differences across parts of the pancreas were evaluated.

Results: In motion phantom scans, conventional DWI led to biased ADC, while motion-compensated waveforms produced consistent ADC. In the breath-held, cardiac-triggered study, conventional DWI led to heterogeneous DW signals and highly variable ADC across the pancreas, whereas motion-compensated DWI avoided these artifacts. In the respiratory-triggered study, conventional DWI produced heterogeneous ADC across the pancreas (head: $1756\pm173\times10^{-6}$mm^2/s; body: $1530\pm338\times10^{-6}$mm^2/s; tail: $1388\pm267\times10^{-6}$mm^2/s), with ADCs in the head significantly higher than in the tail (p<.05). Motion-compensated ADC had lower variability across volunteers (head: $1277\pm102\times10^{-6}$mm^2/s; body: $1204\pm169\times10^{-6}$mm^2/s; tail: $1235\pm178\times10^{-6}$mm^2/s), with no significant difference (p 0.19) across the pancreas.

Conclusion: Cardiovascular motion introduces artifacts and ADC bias in pancreas DWI, which are addressed by motion-robust DWI.

Correspondence: Diego Hernando, PhD, Departments of Radiology and Medical Physics, University of Wisconsin-Madison, Madison, 53705, USA. dhernando@wisc.edu, Twitter: @dherarr.

Keywords

Diffusion-weighted imaging (DWI); pancreas; cardiovascular compression; compressive motion; DWI artifacts

Introduction

Diffusion-weighted imaging (DWI) has the potential to add value in the detection (1–3), diagnosis (4,5), and treatment response prediction of pancreatic diseases (4,6–8). DWI has been shown to have a similar accuracy as contrast-enhanced MRI for the diagnosis of pancreatic cancer and pancreatic neuroendocrine tumors (9). Furthermore, quantitative measurements derived from DW images constitute promising biomarkers for pancreas imaging applications. For example, measurement of the apparent diffusion coefficient (ADC) in the pancreas has been shown to correlate well with histopathological markers, such as the proportion of collagenous fibers (10). Further, ADC measurements may enable differentiation of malignant lesions from healthy tissue (2), mass-forming pancreatitis (11,12), and other benign lesions (13,14). Moreover, recent studies have shown that ADC measurements can help differentiate accessory spleen from small islet cell tumors (11), differentiate near solid serous cystadenomas from neuroendocrine tumors (15), and potentially determine the tumor grade (16,17). DWI has also shown potential to enable an early prediction of treatment response (6–8), as early therapy-induced effects can be reflected in tissue reorganization, changes in cellularity, and vascularization, or metabolic activity, before measurable changes in tumor volume become apparent. Furthermore, DWI can be useful for detecting autoimmune pancreatitis and evaluating the effect of steroid therapy (4). In addition, an increase in tumor ADC values in unresectable pancreatic cancer during chemotherapy predicts better survival (7), pancreatic ductal adenocarcinomas with lower baseline ADC respond poorly to standard chemotherapy and would benefit from intensified treatment (8), and a lower ADC obtained from high b-value DWI in patients with advanced pancreatic cancer may be predictive of early progression in chemotherapy-treated patients (6).

Despite this potential, the ability to differentiate between malignant and benign lesions and to predict treatment response based on ADC measurements remains limited, due to substantial variability and overlap in the quantitative measurements (12,18). ADC values for normal and diseased pancreas have shown a broad variability within studies (6,9,19–22), and substantial overlap in ADC values among normal and diseased pancreas and various tumor grades have been reported (9,22,23). In particular, the reported ADC values for the different parts (head, body, and tail) of the normal pancreas have seen large differences across studies (5,11,19,20,23,24). This overlap and variability in ADC measurements are likely due in part to the presence of multiple technical challenges, particularly physiological motion, that affect DWI of the pancreas. Due to its location within the retroperitoneum, the pancreas may be affected by respiratory, peristaltic, and cardiovascular-related motion (1). The extent of pancreatic motion due to respiration has been studied previously (25), and is routinely addressed in DWI through respiratory triggering (12,26). Further, peristaltic motion can be minimized through the use of gastrointestinal motility inhibitors such as glucagon (27–30).

However, the effect of cardiovascular-related motion, due to both direct cardiac motion and pulsation of large blood vessels, are not understood in the context of DWI of the pancreas. Cardiovascular-induced motion of organs adjacent to the heart (e.g. the liver) or large blood vessels (e.g. the pancreas) occurs throughout the cardiac cycle (31), and therefore its effects may not be fully avoidable using cardiac gating. Conventional DWI is acquired using monopolar DW gradients with elevated motion moments (i.e. motion sensitivity), and generally leads to artifacts in the presence of cardiovascular-induced compressive motion. Indeed, cardiovascular-induced compressive tissue motion often leads to signal dropouts and ADC bias in abdominal organs such as the liver (particularly in the left lobe) (31).

We hypothesize that, similar to the liver, cardiovascular-related motion may lead to artifacts in DWI of the pancreas and thus ADC bias. In current literature, reduction of ADC measurements from pancreatic head to tail has been observed (19,24,32–34). Importantly, the pancreatic head is closest to large blood vessels such as the portal vein, inferior vena cava, aorta, and mesenteric superior artery. Indeed, artery pulsation and other cardiac-related motion may lead to rapid compressive motion of pancreas tissue, leading to signal dropouts and ADC bias in conventional DWI acquisitions performed with monopolar DW gradient waveforms. Thus, the apparent ADC heterogeneity observed across the parts of the healthy pancreas in previous studies may be due to cardiovascular-induced artifacts, analogously to the heterogeneity observed across the liver lobes.

Motion-compensated (MOCO) diffusion-encoding gradient waveforms with nulled first and/or second-order gradient moments (M1, M2) have been proposed to mitigate sensitivity to bulk motion. For example, velocity-compensated (M1= 0) diffusion-encoding gradient waveforms implemented in the liver enable improved ADC reproducibility without cardiac triggering (35,36). Importantly, conventional MOCO diffusion encoding utilizes a multipolar gradient waveform that substantially increases the echo time (TE) compared to monopolar encoding, leading to degraded SNR (37). Optimized methods for motion-robust DWI with minimized TEs have been recently proposed (37–39). These methods generally lead to asymmetric waveforms that optimally utilize the available diffusion encoding time. Although these asymmetric diffusion waveforms may introduce additional challenges (e.g., concomitant gradient effects), these challenges can be often addressed within the optimization formulation itself (e.g., by including a concomitant gradient nulling constraint as performed in this work (39)). By applying optimized motion-compensated DW gradient waveforms, these methods are able to avoid signal dropouts in the presence of cardiovascular-related motion while maximizing SNR, potentially enabling motion-robust DWI. Although motion-robust DWI methods have been demonstrated in various applications of DWI, including in liver (38,39) and cardiac (37) imaging, their performance in the pancreas remains unknown.

Based on these observations, we hypothesize that: 1) cardiovascular-related motion leads to artifacts and bias in conventional DWI of the pancreas, and further 2) these artifacts can be mitigated through the use of recently proposed motion-robust DWI methods. Therefore, the purpose of this work is to evaluate the effects of cardiovascular-related motion on conventional DWI of the pancreas, and to assess the performance of motion-robust DWI methods in a motion phantom and in healthy volunteers.

Methods

In this IRB-approved study conducted with informed written consent, we visualized the effects of cardiovascular-related motion using cardiac-gated cine acquisitions in healthy volunteers. Next, we evaluated these effects in a custom anatomically accurate 3D-printed pancreas motion phantom using DWI under various motion conditions. Finally, we assessed the artifacts and quantified the ADC bias in the pancreas of healthy volunteers using conventional DWI, and evaluated the performance of a recently developed motion-robust DWI method (39). All scanning was performed at 3T (GE Signa Premier) using flexible coils (AIR Technology, GE Healthcare, Waukesha, WI). A safe upper bound of slew rate (150 mT/m/msec) was used for optimization, well below the peak gradient slew rate of 200 mT/m/msec. These acquisitions and analyses are described in detail next.

Visualization of cardiovascular-related pancreas motion

Eight healthy volunteers were scanned with cardiac-gated SSFP of the pancreas in three orthogonal orientations (coronal, parasagittal, and axial) in separate breath-holds to visualize the bulk and compressive motion of the pancreas associated with cardiovascular-related motion. For each orientation, cine images were obtained for 20 frames within the cardiac cycle. For visualization, a radiologist (J.S.) with 9 years of experience in abdominal MRI contoured the pancreas borders on each of the 20 frames acquired within the cardiac cycle.

Evaluation in a motion phantom

Phantom construction: A custom phantom was fabricated for testing motion-compensated diffusion MRI. This phantom consisted of an anthropomorphic hydrogel "pancreas" (see below) embedded in silicone (40). Polyacrylamide hydrogel was used for the pancreas model in order to enable tissue-mimicking compressive motion. To create the anthropomorphic hydrogel model, the pancreas was segmented from a set of T2-weighted MR images of a healthy volunteer and a 3D digital model of the pancreas was exported in STL format. The model was first 3D-printed with polyvinyl-alcohol (PVA) filament on an Ultimaker (Utrecht, Netherlands) S5 machine. The PVA pancreas was then coated in liquid latex rubber. Once the rubber coating had dried, the inner PVA pancreas volume was dissolved with water, leaving a pancreas-shaped void in a rubber shell. Hydrogel with 8% acrylamide/bis-acrylamide concentration was then poured into the rubber mold and allowed to polymerize. Once cured, the hydrogel pancreas was extracted from the rubber, placed in a water-tight container, and surrounded with silicone. Compliant tubing was then run over the top of the pancreas model and fixed within the water-tight container filled with silicone (see Supporting Information Video S1). The ends of the tubing were then integrated into a flow loop with a pulsatile positive displacement pump (BDC PD-1100, BDC Laboratories, Wheat Ridge, CO).

Motion setup: Water was pumped through the system, causing deformation of the compliant tube and adjacent hydrogel pancreas model at a frequency of one hertz. This setup was intended to mimic the cyclic motion induced by the cardiovascular-induced compressive motion of the vessels surrounding the pancreas in-vivo, as shown in the videos in Supporting Information Video S1. A phantom similar to the one in the photograph was used, with

opaque silicone surroundings and pancreas neck placed between the tube and the container bottom to facilitate compressive motion in the pancreas. The videos show increased flow amplitude leads to increased pulsation of the tube, causing more severe deformation of the pancreas model.

Acquisition: At various flow velocities (0.5, 1.0, 1.5, 2.0, 2.5, 3.0, 3.5, 4.0 liters/min), DW images using standard monopolar (TE = 49 ms) and optimized motion-compensated (TE = 65 ms) waveforms were acquired. Motion-compensated waveforms were designed using the Optimized Diffusion-weighting Gradient waveform Design (ODGD) method (39). In this work, ODGD was used to achieve the desired b-values with minimum TE, first order motion moment nulling and concomitant gradient (CG) nulling. For each type of gradient waveforms (monopolar and motion-compensated), three orthogonal diffusion directions were obtained, each with two b values (b = 50, 500 s/mm^2, with 2 and 4 repetitions, respectively).

Analysis: One representative slice containing the head, body, and tail of the pancreas model was selected. The DW images and ADC maps were compared between standard monopolar and motion-compensated DW waveforms, in the absence of motion, as well as in the presence of various levels of motion. The histograms of the ADC values in the pancreas segmented within the selected slice were generated, with mean and standard deviation calculated for each histogram, to compare the ADC distributions of both waveforms.

Characterization and correction of motion artifacts in vivo

Evaluating single-slice breath-held cardiac-gated DWI:

Characterization under various cardiac trigger delays: The same eight healthy volunteers scanned for the visualization of cardiovascular-related pancreas motion, were scanned with standard monopolar diffusion waveforms. To maximally control the acquisition timing relative to the cardiac cycle, single-slice DWI was acquired using breath-holding and cardiac (peripheral) gating. Based on the observations from the SSFP images, one axial slice that captured the compressive motion of adjacent vessels on the pancreatic head and one axial slice that captured most of the rest of the pancreas were used for DWI. DW images were acquired in a single end-of-expiration breath-hold. This acquisition was repeated at three cardiac trigger delays (20, 100, and 200 ms after the R wave), and in three diffusion directions using a standard monopolar waveform (TE = 50 ms), for a total of 9 breath-held monopolar DWI acquisitions per volunteer. Reduced field-of-view (41,42) (readout × phase encode FOV = 32 cm × 12.8 cm) was used with spatial resolution of 2 mm × 2 mm × 5 mm, with b = 50, 500 s/mm^2.

Correction using motion-compensated DW waveforms: The same eight volunteers were scanned within the same exams as above, in order to evaluate the performance of motion-compensated DW waveforms. Single-slice DWI using a motion-compensated gradient waveform (first order moment nulled with CG nulling, TE = 72 ms) (39) was tested using the same parameters as the standard monopolar waveform, with trigger delay = 20 ms. Three breath-held acquisitions were performed, one per diffusion direction. Other trigger delays were not included due to scan time limitations.

Evaluating whole-pancreas respiratory-triggered DWI: In order to evaluate clinically relevant whole-pancreas DWI acquisitions, ten healthy volunteers (with an overlap of 6 volunteers from the previous scans) were scanned. Whole-pancreas DWI was acquired using respiratory-triggering with parameters similar to our local clinical protocol, including three diffusion directions, with b = 50, 500 s/mm^2. Two separate acquisitions were performed, using standard monopolar and motion-compensated gradient waveforms, respectively. The approximate acquisition time was 4 minutes. Detailed information on imaging parameters is shown in Table 1. A triggering window of 30% was used to acquire all slices covering the pancreas in one respiratory interval.

Image analysis and measurements: ADC measurements were performed in both single-slice and whole-pancreas DWI acquisitions, each for both standard monopolar and motion-compensated diffusion waveforms. For the single-slice study, region of interest (ROI) measurements were performed on ADC maps derived from each combination of cardiac trigger delay and diffusion direction to characterize the effects of cardiovascular-related motion. Oval ROIs were drawn by a radiologist (JS) in the pancreatic head, body, and tail in the b = 50 s/mm^2 DWI images (with b = 0 s/mm^2 as an anatomical reference), then copied to the corresponding ADC map for measurement, to avoid reader bias in directly placing ROIs in the ADC maps. For the whole-pancreas study, ROI measurements were performed on ADC maps derived from the averaged DW images of all diffusion directions. Oval ROIs were drawn on the slice that included most of each pancreatic part in the b = 50 s/mm^2 DWI images (with b = 0 s/mm^2 as an anatomical reference), then copied to the corresponding ADC map for measurement. For both studies, ROIs were drawn as large as possible in each pancreatic part while avoiding peripheral regions with susceptibility artifacts, resulting in ROI areas between 52 and 244 mm^2.

Statistical analysis: Paired *T*-tests were performed to evaluate the ADC differences in different parts of the pancreas for both standard monopolar and motion-compensated waveforms.

Effect of peristalsis: Single repetitions taken within the same breath-hold and at the same cardiac trigger delay were compared qualitatively to assess the presence of non-cardiovascular-related motion artifacts in the acquired pancreas DWI images.

Results

Visualization of cardiovascular-related pancreas motion

Cardiac-gated dynamic SSFP images of the pancreas in coronal, parasagittal, and axial views are shown in Supporting Information Video S2. Pulsation of the aorta, as well as motion near the portal vein, inferior vena cava, and splenic vein caused substantial translational and compressive motion of the pancreatic head and body.

Evaluation in a motion phantom

Figure 1 shows DW images and ADC maps of the pancreas motion phantom using both the standard monopolar and motion-compensated DW waveforms. In the absence of substantial

motion (zero or low flow amplitude in the tube), the ADC distributions were similar between the two waveforms. In the presence of motion, the standard monopolar DW waveforms led to artifacts in both b = 50 s/mm^2 and b = 500 s/mm^2 images, as well as biased (overestimated) ADC values. The severity and extension of the artifacts and ADC bias increased with larger flow amplitude. In contrast, with motion-compensated DW waveforms, the DW signals appeared consistent regardless of the presence of motion. Further, motion-compensated DW waveforms produced consistent and spatially uniform ADC values throughout the hydrogel pancreas model, over a wide range of flow amplitudes.

Characterization and correction of motion artifacts in vivo

Characterization under various cardiac trigger delays: In the breath-hold study, signal dropouts occurred in DW images in all three parts of the pancreas, in all diffusion directions, and at all acquired trigger delay times. DW images of b = 500 s/mm^2 in the pancreatic head, body, and tail are shown in Figure 2. Contours were drawn on the b = 0 images and overlaid onto the b = 500 s/mm^2 images to indicate the location of the pancreatic head. For each acquisition and each part of the pancreas, the mean and standard deviation of the ADC measured across volunteers are noted in each sub-image. Signal dropouts were consistent across repetitions acquired with the same cardiac phase and diffusion direction. However, dropouts appeared at different locations for images acquired at different cardiac phases (trigger delays) or in different diffusion directions. As a result of artifacts in DW images, biased ADC values with a large variation across volunteers occurred for all trigger delays and diffusion directions (Supporting Information Figure S1).

Correction using motion-compensated DW waveforms: With standard monopolar DW waveforms, heterogeneous DW signals and ADC values occurred across the pancreas for all diffusion directions (Figure 2). The measured ADCs had a large variability across volunteers in all three diffusion directions at a trigger delay time of 20 ms (the range of standard deviation across volunteers is $354 - 1590 \times 10^{-6}$ mm^2/s for all parts of the pancreas and in all diffusion directions). Heterogeneous ADCs across the parts of the pancreas were observed, with significantly higher ADC in the head than in the tail ($p < .05$) in two of the diffusion directions (RL and AP) (Figure 3). Using a motion-compensated DW waveform, DW signals and ADC values were uniform across the parts of the pancreas (Figure 3), and the measured ADCs had a much lower variability across volunteers (the standard deviation of ADC across volunteers is $63 - 279 \times 10^{-6}$ mm^2/s for all parts of the pancreas and in all diffusion directions). Finally, motion-compensated DW waveforms led to comparable ADC in all three parts of pancreas, as shown in Figure 4.

Evaluating whole-pancreas respiratory-triggered DWI: Figure 5 shows examples of DWI b = 500 s/mm^2 images and ADC maps acquired with respiratory-triggering using standard monopolar and motion-compensated DW waveforms. Standard DW waveforms led to localized regions of signal dropouts, resulting in heterogeneous ADC values across the three parts of the pancreas. The mean ADC values for the pancreatic head was $1756 \pm 173 \times 10^{-6}$ mm^2/s and the median (IQR) was 1739 (1638 to 1856) $\times 10^{-6}$ mm^2/s. For the pancreatic body: $1530 \pm 338 \times 10^{-6}$ mm^2/s and 1468 (1229 to 1938) $\times 10^{-6}$ mm^2/s. And for the pancreatic tail: $1388 \pm 267 \times 10^{-6}$ mm^2/s and 1264 (1187 to 1598) $\times 10^{-6}$ mm^2/s. Using a

motion-compensated DW waveform, the measured ADCs were comparable across the parts of the pancreas (head: $1277 \pm 102 \times 10^{-6}$ mm^2/s; body: $1204 \pm 169 \times 10^{-6}$ mm^2/s; tail: $1235 \pm 178 \times 10^{-6}$ mm^2/s). Boxplots of ADC measurements of eight volunteers for the two waveforms in respiratory-triggered study are shown in Figure 6. Using a standard monopolar DW waveform, the measured ADCs in the pancreatic head and body were significantly higher than in the tail ($p < .05$). Using motion-compensated DW waveforms, the measured ADCs had a lower variability among volunteers and were comparable in all three parts of pancreas ($p = .54$ between head and tail, $p = .69$ between body and tail, and $p = .19$ between head and body).

Effect of peristalsis: The effect of additional sources of motion artifacts (e.g. peristalsis) in breath-held, cardiac-triggered multi-repetition DWI was evaluated qualitatively. Examples of individual repetitions of single-slice diffusion-weighted images with b = 0, 50, and 500 s/mm^2 in the SI diffusion direction, at cardiac (peripheral-gating) trigger delay of 20 ms are shown in Supporting Information Video S3. In the standard monopolar DW images, the location of signal dropout regions appears largely consistent across repetitions within the same breath-hold. However, residual variability across repetitions may be present, as indicated by the yellow arrows. DW images across multiple repetitions appeared similar when using motion-compensated waveforms.

Discussion

Cardiovascular-related motion leads to artifacts and bias in conventional DWI of the pancreas. These artifacts and bias are mitigated through the use of recently proposed motion-robust DWI methods. Cardiovascular-related motion induces complex compressive motion of the pancreas, leading to signal dropouts in head, body, and tail, at various phases in the cardiac cycle, and in various diffusion directions. Motion-compensated diffusion gradient waveforms improved the DW signal reliability, resulting in more reproducible diffusion quantification.

These results may have important implications for research and clinical applications of pancreas DWI. As a result of artifacts in DW images, biased ADC values with a large variation across volunteers occurred in all cases. Importantly, these artifacts and bias are likely unavoidable by simply selecting a particular diffusion direction or trigger delay. A large location and subject dependence on the occurrence of the artifacts was observed across different trigger delays. At the same trigger delay, signal void artifacts occurred at different slices for different subjects. Beyond the long scan times that would be needed for cardiac- and respiratory-triggered DWI of the pancreas, our proof of concept study suggests that there may not be an optimal cardiac trigger delay across slices and subjects. These results highlight the value of motion-compensated gradient waveforms to provide consistent ADC values across slices and subjects. Motion-robust DWI may reduce ADC bias and variability in the clinic, with the potential to enable more accurate lesion detection and diagnosis, as well as lesion characterization (e.g., for distinguishing benign versus malignant lesions) and treatment monitoring.

Cardiovascular-induced compressive motion is a major source of the signal dropouts observed in pancreas DWI. The phantom study suggested that pulsation or motion within blood vessels may induce pancreas deformation, and increased deformation led to increased severity of DWI artifacts and ADC bias. Further, in the highly controlled cardiac triggered *in vivo* experiments using monopolar DW gradients, individual repetitions were examined qualitatively. Importantly, for a BH acquisition with a fixed cardiac trigger delay (TD) time, the location of the artifacts appeared consistent across repetitions. Also, the location of artifacts appears different for different acquisitions performed at different TDs or different diffusion directions. Therefore, the effect is likely to be highly periodic with the cardiac cycle, which strongly suggests that the source is cardiovascular-related motion. Nevertheless, additional sources of motion (e.g., peristalsis) may contribute to the observed artifacts. Regardless of the specific source of motion, this study demonstrated the potential for improved ADC reproducibility with motion compensated gradients.

Using monopolar diffusion waveforms showed heterogeneity of ADC measurements from pancreatic head to tail (higher ADC in the head, and lower in the tail), which replicates the results from various previous studies (19,24,32–34). One previous study reported that ADC values in the pancreatic head were higher than in the tail, independently of gender, age and BMI (34). Schennagel et al. proposed the cause for the different ADC values in pancreatic head, neck, and tail to be due to the heterogeneity of the pancreatic tissue composition. However, our results suggest that these differences may be artifactual and due to cardiovascular-related motion effects. Importantly, in our study, this heterogeneity in ADC across different parts of pancreas disappeared when using motion-compensated gradient waveforms.

The motion artifact correction achieved by motion-compensated gradient waveforms in pancreas DWI bears resemblance to that in other organs. The effects of motion-compensated gradient waveforms to mitigate motion-induced ADC biases have been demonstrated in the liver MRI literature (37–39). In previous studies, monopolar-based ADC showed significant bias in the left lobe relative to the right lobe due to its sensitivity to motion, while DWI with motion-compensated waveforms showed no significant ADC bias in the left lobe relative to the right lobe, demonstrating robustness to cardiac-induced motion (37–39).

The observed ADC bias with monopolar DW waveforms was larger in the highly-controlled cardiac-triggered, breath-held acquisitions than in the respiratory triggered study. This is likely due to the high consistency of signal dropouts across repetitions in cardiac-triggered, breath-held acquisitions. In contrast, in the respiratory-triggered acquisitions without cardiac triggering, many repetitions are acquired at different cardiac phases, which partially averages out these signal dropouts, and leads to less pronounced (although still substantial) ADC bias. Another possible difference is that cardiovascular-related compressive motion may actually be different during a breath-hold compared to during free breathing. Before holding their breath, volunteers were coached to take two rounds of deep inspiration and expiration, as practiced in the clinic. Previous studies show that the diameters of portal, splenic, and superior mesenteric veins (major veins by the pancreas) change significantly between deep inspiration and expiration (43), which may have resulted in stronger venous dilation and contraction, and increased compressive tissue motion. However, even in

respiratory-triggered acquisitions the ADC bias and variability are still large and likely to interfere with quantitative applications of ADC, such as lesion characterization. Importantly, this bias and variability are reduced substantially with motion-compensated methods.

This study had several limitations. Since our study only included healthy volunteers, further studies in patients are needed. Our results suggest that motion compensation may improve the precision (e.g. test-retest repeatability) of ADC measurements in the pancreas (44). However, assessment of repeatability was not directly performed in this work. Further studies in volunteers and patients may also be needed to establish a clear separation of the effects of tissue composition and motion artifacts. With reduced motion-induced artifacts as enabled by motion-robust DWI methods, tissue heterogeneity may be more accurately measured in subsequent studies. The motion phantom used in this work does not precisely replicate the complex physiological motion of the pancreas. However, this phantom enables the evaluation of diffusion-weighted imaging under highly-controlled pulsatile motion. Remaining challenges in pancreas DWI are not addressed in this study, including susceptibility-related distortions which may influence image quality, as well as non-Gaussian diffusion which may require more advanced modeling of DW signals (45–48). Nevertheless, the proposed motion-robust methods are compatible with other advances in DWI, including low-distortion techniques (41,49,50), and the improved signal reliability provided by motion-compensated DW waveforms may also enable improved performance of advanced diffusion modeling methods. Remaining systematic differences may exist between the ADC values derived from monopolar and motion-compensated waveforms, likely due to multiple effects including IVIM (micro-perfusion) (51–53), echo time, and diffusion time. For instance, motion-compensated diffusion acquisitions may lead to residual IVIM-induced dependence of pancreas ADC measurements on the choice of b values. This dependence of ADC on the choice of b values is expected to be different for motion-compensated compared to monopolar-based ADC measurements (Supporting Information Figure S2). Thorough analysis of these multiple potential confounding effects is beyond the scope of this work. One future consideration for deploying this technique across scanners is increased minimum TR due to issues including gradient duty cycle and heating limitations, which may lead to longer overall scan time (e.g. when the number of slices required to cover the whole liver is large). Importantly, compared to monopolar diffusion waveforms, motion-compensated waveforms enable improved ADC mapping in the pancreas by reducing motion-related bias and variability.

Conclusion

Cardiovascular-related compressive motion introduces substantial artifacts and ADC bias in pancreas DWI, which can be addressed by motion-compensated diffusion gradient waveforms. These results may have important implications both for understanding the current literature on DWI of the pancreas and for the design of improved DWI techniques for clinical and research applications.

Supplementary Material

Refer to Web version on PubMed Central for supplementary material.

Acknowledgements

References

1. Ichikawa T, Erturk SM, Motosugi U, et al. High-b Value Diffusion-Weighted MRI for Detecting Pancreatic Adenocarcinoma: Preliminary Results. Am J Roentgenol. 2007;188(2):409–414. doi:10.2214/AJR.05.1918 [PubMed: 17242249]

2. Brenner R, Metens T, Bali M, Demetter P, Matos C. Pancreatic neuroendocrine tumor: Added value of fusion of T2-weighted imaging and high b-value diffusion-weighted imaging for tumor detection. Eur J Radiol. 2012;81(5):e746–e749. doi:10.1016/j.ejrad.2012.01.032 [PubMed: 22386133]

3. Schmid-Tannwald C, Schmid-Tannwald CM, Morelli JN, et al. Comparison of abdominal MRI with diffusion-weighted imaging to 68Ga-DOTATATE PET/CT in detection of neuroendocrine tumors of the pancreas. Eur J Nucl Med Mol Imaging. 2013;40(6):897–907. doi:10.1007/s00259-013-2371-5 [PubMed: 23460395]

4. Kamisawa T, Takuma K, Anjiki H, et al. Differentiation of autoimmune pancreatitis from pancreatic cancer by diffusion-weighted MRI. Am J Gastroenterol. 2010;105(8):1870–1875. doi:10.1038/ajg.2010.87 [PubMed: 20216538]

5. Fattahi R, Balci NC, Perman WH, et al. Pancreatic diffusion-weighted imaging (DWI): comparison between mass-forming focal pancreatitis (FP), pancreatic cancer (PC), and normal pancreas. J Magn Reson Imaging JMRI. 2009;29(2):350–356. doi:10.1002/jmri.21651 [PubMed: 19161187]

6. Niwa T, Ueno M, Ohkawa S, et al. Advanced pancreatic cancer: the use of the apparent diffusion coefficient to predict response to chemotherapy. Br J Radiol. 2009;82(973):28–34. doi:10.1259/bjr/43911400 [PubMed: 19095814]

7. Nishiofuku H, Tanaka T, Marugami N, et al. Increased tumour ADC value during chemotherapy predicts improved survival in unresectable pancreatic cancer. Eur Radiol. 2016;26:1835–1842. doi:10.1007/s00330-015-3999-2 [PubMed: 26385808]

8. Trajkovic-Arsic M, Heid I, Steiger K, et al. Apparent Diffusion Coefficient (ADC) predicts therapy response in pancreatic ductal adenocarcinoma. Sci Rep. 2017;7(1):17038. doi:10.1038/s41598-017-16826-z [PubMed: 29213099]

9. Kartalis N, Lindholm TL, Aspelin P, Permert J, Albiin N. Diffusion-weighted magnetic resonance imaging of pancreas tumours. Eur Radiol. 2009;19(8):1981–1990. doi:10.1007/s00330-009-1384-8 [PubMed: 19308414]

10. Muraoka N, Uematsu H, Kimura H, et al. Apparent diffusion coefficient in pancreatic cancer: characterization and histopathological correlations. J Magn Reson Imaging JMRI. 2008;27(6):1302–1308. doi:10.1002/jmri.21340 [PubMed: 18504750]

11. Lee SS, Byun JH, Park BJ, et al. Quantitative analysis of diffusion-weighted magnetic resonance imaging of the pancreas: usefulness in characterizing solid pancreatic masses. J Magn Reson Imaging JMRI. 2008;28(4):928–936. doi:10.1002/jmri.21508 [PubMed: 18821618]

12. Sandrasegaran K, Nutakki K, Tahir B, Dhanabal A, Tann M, Cote GA. Use of diffusion-weighted MRI to differentiate chronic pancreatitis from pancreatic cancer. AJR Am J Roentgenol. 2013;201(5):1002–1008. doi:10.2214/AJR.12.10170 [PubMed: 24147470]

13. d'Assignies G, Fina P, Bruno O, et al. High sensitivity of diffusion-weighted MR imaging for the detection of liver metastases from neuroendocrine tumors: comparison with T2-weighted and

dynamic gadolinium-enhanced MR imaging. Radiology. 2013;268(2):390–399. doi:10.1148/radiol.13121628 [PubMed: 23533288]

14. Warda MHA, Hasan DI, Elteeh OA. Differentiation of Pancreatic lesions using Diffusion-Weighted MRI. Egypt J Radiol Nucl Med. 2015;46(3):563–568. doi:10.1016/j.ejrnm.2015.03.009

15. Jang KM, Kim SH, Song KD, Kim YK, Lee SJ, Choi D. Differentiation of solid-type serous cystic neoplasm from neuroendocrine tumour in the pancreas: value of abdominal MRI with diffusion-weighted imaging in comparison with MDCT. Clin Radiol. 2015;70(2):153–160. doi:10.1016/j.crad.2014.10.010 [PubMed: 25465293]

16. Jang KM, Kim SH, Lee SJ, Choi D. The value of gadoxetic acid-enhanced and diffusion-weighted MRI for prediction of grading of pancreatic neuroendocrine tumors. Acta Radiol Stockh Swed 1987. 2014;55(2):140–148. doi:10.1177/0284185113494982

17. Hwang EJ, Lee JM, Yoon JH, et al. Intravoxel incoherent motion diffusion-weighted imaging of pancreatic neuroendocrine tumors: prediction of the histologic grade using pure diffusion coefficient and tumor size. Invest Radiol. 2014;49(6):396–402. doi:10.1097/RLI.0000000000000028 [PubMed: 24500090]

18. Bozgeyik Z, Onur MR, Poyraz AK. The role of diffusion weighted magnetic resonance imaging in oncologic settings. Quant Imaging Med Surg. 2013;3(5):269–278. doi:10.3978/j.issn.2223-4292.2013.10.07 [PubMed: 24273745]

19. Ding X, Xu H, Zhou J, et al. Reproducibility of normalized apparent diffusion coefficient measurements on 3.0-T diffusion-weighted imaging of normal pancreas in a healthy population. Medicine (Baltimore). 2019;98(14). doi:10.1097/MD.0000000000015104

20. Barral M, Soyer P, Ben Hassen W, et al. Diffusion-weighted MR imaging of the normal pancreas: reproducibility and variations of apparent diffusion coefficient measurement at 1.5- and 3.0-Tesla. Diagn Interv Imaging. 2013;94(4):418–427. doi:10.1016/j.diii.2012.12.007 [PubMed: 23415463]

21. Wang Y, Chen ZE, Nikolaidis P, et al. Diffusion-weighted magnetic resonance imaging of pancreatic adenocarcinomas: Association with histopathology and tumor grade. J Magn Reson Imaging. 2011;33(1):136–142. doi:10.1002/jmri.22414 [PubMed: 21182131]

22. Lemke A, Laun FB, Klauss M, et al. Differentiation of pancreas carcinoma from healthy pancreatic tissue using multiple b-values: comparison of apparent diffusion coefficient and intravoxel incoherent motion derived parameters. Invest Radiol. 2009;44(12):769–775. doi:10.1097/RLI.0b013e3181b62271 [PubMed: 19838121]

23. Wang Y, Miller FH, Chen ZE, et al. Diffusion-weighted MR imaging of solid and cystic lesions of the pancreas. Radiogr Rev Publ Radiol Soc N Am Inc. 2011;31(3):E47–64. doi:10.1148/rg.313105174

24. Yoshikawa T, Kawamitsu H, Mitchell DG, et al. ADC Measurement of Abdominal Organs and Lesions Using Parallel Imaging Technique. Am J Roentgenol. 2006;187(6):1521–1530. doi:10.2214/AJR.05.0778 [PubMed: 17114546]

25. Langen KM, Jones DTL. Organ motion and its management. Int J Radiat Oncol. 2001;50(1):265–278. doi:10.1016/S0360-3016(01)01453-5

26. Balci NC, Perman WH, Saglam S, Akisik F, Fattahi R, Bilgin M. Diffusion-weighted magnetic resonance imaging of the pancreas. Top Magn Reson Imaging TMRI. 2009;20(1):43–47. doi:10.1097/RMR.0b013e3181b48667 [PubMed: 19687725]

27. Barral M, Taouli B, Guiu B, et al. Diffusion-weighted MR Imaging of the Pancreas: Current Status and Recommendations. Radiology. 2014;274(1):45–63. doi:10.1148/radiol.14130778

28. Kwee TC, Takahara T, Koh D-M, Nievelstein RAJ, Luijten PR. Comparison and reproducibility of ADC measurements in breathhold, respiratory triggered, and free-breathing diffusion-weighted MR imaging of the liver. J Magn Reson Imaging JMRI. 2008;28(5):1141–1148. doi:10.1002/jmri.21569 [PubMed: 18972355]

29. Kandpal H, Sharma R, Madhusudhan KS, Kapoor KS. Respiratory-Triggered Versus Breath-Hold Diffusion-Weighted MRI of Liver Lesions: Comparison of Image Quality and Apparent Diffusion Coefficient Values. Am J Roentgenol. 2009;192(4):915–922. doi:10.2214/AJR.08.1260 [PubMed: 19304695]

30. Mochiki E, Suzuki H, Takenoshita S, et al. Mechanism of inhibitory effect of glucagon on gastrointestinal motility and cause of side effects of glucagon. J Gastroenterol. 1998;33(6):835–841. doi:10.1007/s005350050184 [PubMed: 9853556]

31. Liau J, Lee J, Schroeder ME, Sirlin CB, Bydder M. Cardiac motion in diffusion-weighted MRI of the liver: artifact and a method of correction. J Magn Reson Imaging. 2012;35(2):318–327. doi:10.1002/jmri.22816 [PubMed: 21959926]

32. Schoennagel BP, Habermann CR, Roesch M, et al. Diffusion-weighted imaging of the healthy pancreas: Apparent diffusion coefficient values of the normal head, body, and tail calculated from different sets of b-values. J Magn Reson Imaging. 2011;34(4):861–865. doi:10.1002/jmri.22743 [PubMed: 21837782]

33. Dale BM, Braithwaite AC, Boll DT, Merkle EM. Field Strength and Diffusion Encoding Technique Affect the Apparent Diffusion Coefficient Measurements in Diffusion-Weighted Imaging of the Abdomen. Invest Radiol. 2010;45(2):104–108. doi:10.1097/RLI.0b013e3181c8ceac [PubMed: 20027117]

34. Kiani Nazarlou A, Faeghi F, Abdkarimi MH, Asghari JafarAbadi M. ADC values in diffusion-weighted MRI and their relationship with age, gender and BMI in healthy people's pancreases. Br J Radiol. 2015;88(1047). doi:10.1259/bjr.20140449

35. Kwee TC, Takahara T, Ochiai R, Nievelstein RAJ, Luijten PR. Diffusion-weighted whole-body imaging with background body signal suppression (DWIBS): features and potential applications in oncology. Eur Radiol. 2008;18(9):1937–1952. doi:10.1007/s00330-008-0968-z [PubMed: 18446344]

36. Ozaki M, Inoue Y, Miyati T, et al. Motion artifact reduction of diffusion-weighted MRI of the liver: Use of velocity-compensated diffusion gradients combined with tetrahedral gradients. J Magn Reson Imaging. 2013;37(1):172–178. doi:10.1002/jmri.23796 [PubMed: 22987784]

37. Aliotta E, Wu HH, Ennis DB. Convex optimized diffusion encoding (CODE) gradient waveforms for minimum echo time and bulk motion-compensated diffusion-weighted MRI. Magn Reson Med. 2017;77(2):717–729. doi:10.1002/mrm.26166 [PubMed: 26900872]

38. Zhang Y, Peña-Nogales Ó, Holmes JH, Hernando D. Motion-robust and blood-suppressed M1-optimized diffusion MR imaging of the liver. Magn Reson Med. 2019;82(1):302–311. doi:10.1002/mrm.27735 [PubMed: 30859628]

39. Peña-Nogales Ó, Zhang Y, Wang X, et al. Optimized Diffusion-Weighting Gradient Waveform Design (ODGD) formulation for motion compensation and concomitant gradient nulling. Magn Reson Med. 2019;81(2):989–1003. doi:10.1002/mrm.27462 [PubMed: 30394568]

40. Rutkowski DR, Kim C, Roldán-Alzate A. Hydrogel-based phantoms for magnetic resonance imaging. Proc Summer Biomech Bioeng Biotransport Conf. (SB3C2020) #376.

41. Ma C, Li Y, Pan C, et al. High resolution diffusion weighted magnetic resonance imaging of the pancreas using reduced field of view single-shot echo-planar imaging at 3 T. Magn Reson Imaging. 2014;32(2):125–131. doi:10.1016/j.mri.2013.10.005 [PubMed: 24231348]

42. Kim H, Lee JM, Yoon JH, et al. Reduced Field-of-View Diffusion-Weighted Magnetic Resonance Imaging of the Pancreas: Comparison with Conventional Single-Shot Echo-Planar Imaging. Korean J Radiol. 2015;16(6):1216–1225. doi:10.3348/kjr.2015.16.6.1216 [PubMed: 26576110]

43. Goyal AK, Pokharna DS, Sharma SK. Ultrasonic measurements of portal vasculature in diagnosis of portal hypertension. A controversial subject reviewed. J Ultrasound Med Off J Am Inst Ultrasound Med. 1990;9(1):45–48. doi:10.7863/jum.1990.9.1.45

44. Starekova J, Geng R, Pirasteh A, Wang Z, Zhang Y, Hernando D. Improved Repeatability of Abdominal Diffusion MRI using Motion-Compensated Methods. 106th Sci Assem Annu Meet Radiol Soc N Am. (RSNA2020) #20011881.

45. Le Bihan D, Breton E, Lallemand D, Aubin ML, Vignaud J, Laval-Jeantet M. Separation of diffusion and perfusion in intravoxel incoherent motion MR imaging. Radiology. 1988;168(2):497–505. doi:10.1148/radiology.168.2.3393671 [PubMed: 3393671]

46. Mulkern RV, Gudbjartsson H, Westin CF, et al. Multi-component apparent diffusion coefficients in human brain. NMR Biomed. 1999;12(1):51–62. doi:10.1002/(sici)1099-1492(199902)12:1<51::aid-nbm546>3.0.co;2-e [PubMed: 10195330]

47. Bennett KM, Schmainda KM, Bennett (Tong) R, Rowe DB, Lu H, Hyde JS. Characterization of continuously distributed cortical water diffusion rates with a stretched-exponential model. Magn Reson Med. 2003;50(4):727–734. doi:10.1002/mrm.10581 [PubMed: 14523958]

48. Jensen JH, Helpern JA, Ramani A, Lu H, Kaczynski K. Diffusional kurtosis imaging: the quantification of non-gaussian water diffusion by means of magnetic resonance imaging. Magn Reson Med. 2005;53(6):1432–1440. doi:10.1002/mrm.20508 [PubMed: 15906300]

49. Saritas EU, Cunningham CH, Lee JH, Han ET, Nishimura DG. DWI of the spinal cord with reduced FOV single-shot EPI. Magn Reson Med. 2008;60(2):468–473. doi:10.1002/mrm.21640 [PubMed: 18666126]

50. Chen N- K, Guidon A, Chang H-C, Song AW. A robust multi-shot scan strategy for high-resolution diffusion weighted MRI enabled by multiplexed sensitivity-encoding (MUSE). NeuroImage. 2013;72:41–47. doi:10.1016/j.neuroimage.2013.01.038 [PubMed: 23370063]

51. Ahlgren A, Knutsson L, Wirestam R, et al. Quantification of microcirculatory parameters by joint analysis of flow-compensated and non-flow-compensated intravoxel incoherent motion (IVIM) data. Nmr Biomed. 2016;29(5):640–649. doi:10.1002/nbm.3505 [PubMed: 26952166]

52. Wetscherek A, Stieltjes B, Laun FB. Flow-compensated intravoxel incoherent motion diffusion imaging. Magn Reson Med. 2015;74(2):410–419. doi:10.1002/mrm.25410 [PubMed: 25116325]

53. Moulin K, Aliotta E, Ennis DB. Effect of flow-encoding strength on intravoxel incoherent motion in the liver. Magn Reson Med. 2019;81(3):1521–1533. doi:10.1002/mrm.27490 [PubMed: 30276853]
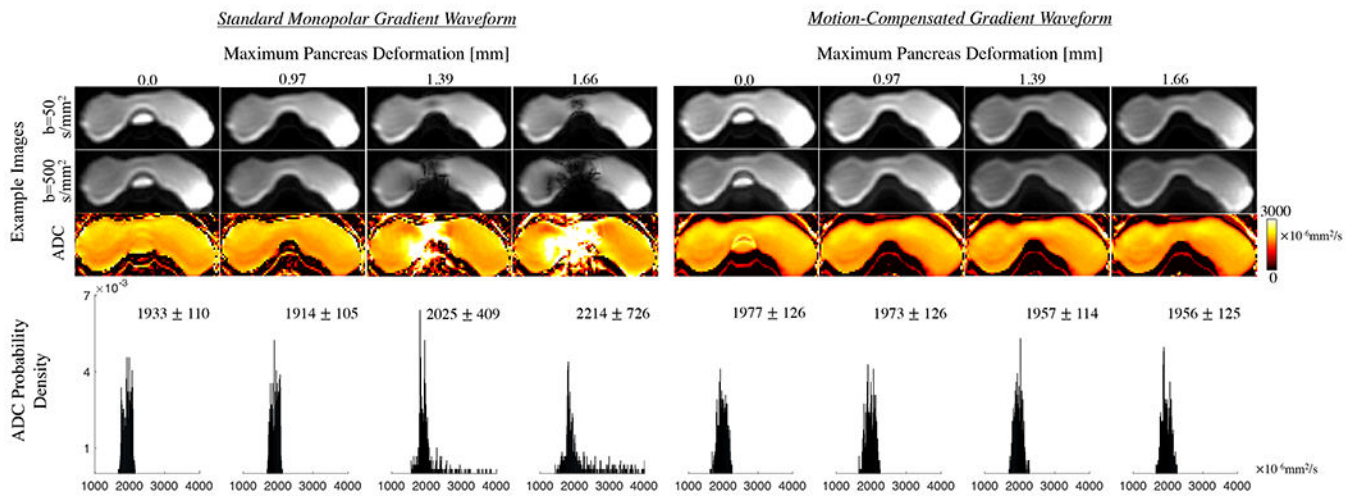
Figure 1.

DW images and ADC maps of the pancreas motion phantom using both the standard monopolar and motion-compensated DW waveforms. With the standard monopolar DW waveforms, artifacts appeared in both $b = 50$ s/mm^2 and $b = 500$ s/mm^2 images, resulting in overestimated ADC values. The severity and extension of the artifacts and ADC bias increased with larger flow amplitude in the tube. With motion-compensated DW waveforms, however, the signals in the DW images appeared consistent, producing uniform ADC values throughout the pancreas hydrogel model. With no or small pancreas deformation, the ADC distributions were similar between the two waveforms. However, with large deformation, the ADC histograms from standard waveforms were broader and shifted to higher ADC values. With motion-compensated waveforms, DW images and ADC distributions were similar regardless of the pancreas motion.
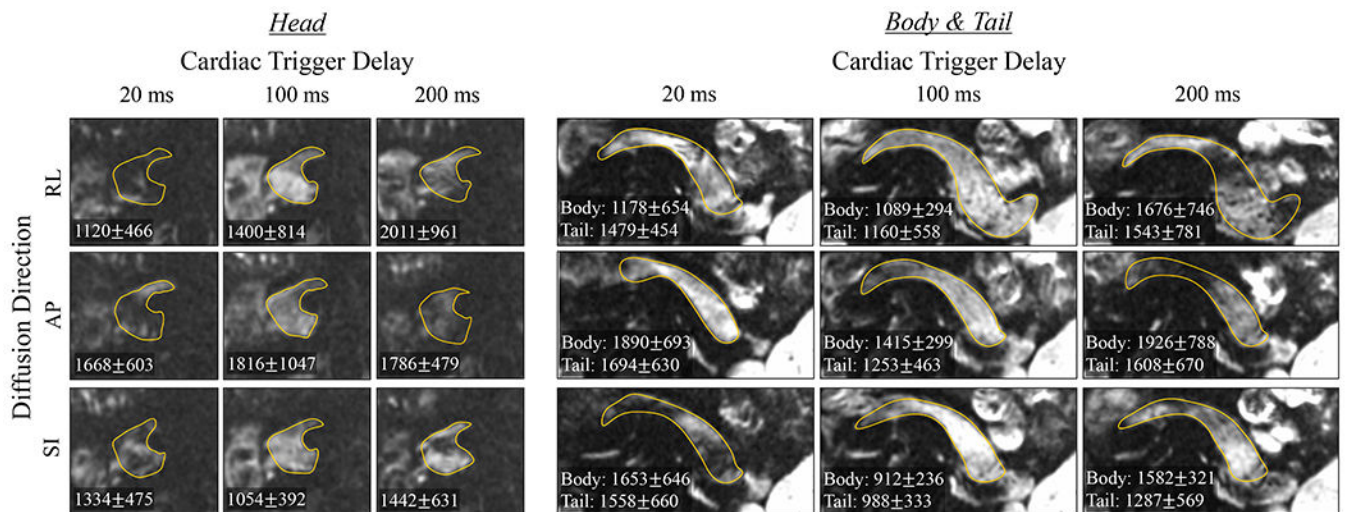
Figure 2.

Single-slice monopolar-based diffusion-weighted images with b = 500 s/mm^2 in three diffusion directions. DWI was obtained at three different cardiac trigger delays, each acquired in a separate breath hold. The yellow contours were drawn from the T2-weighted image (b = 0 s/mm^2, not shown) and overlaid on DWI b = 500 s/mm^2 to indicate pancreas location. For each acquisition and each part of the pancreas, the mean and standard deviation of the ADC measured across volunteers are noted in each sub-image. Using monopolar DW gradients, signal dropouts occurred in DWI images in all three parts of the pancreas, in all diffusion directions, and at all trigger delay times, resulting in biased ADC values with a large variation across volunteers observed for each acquisition.
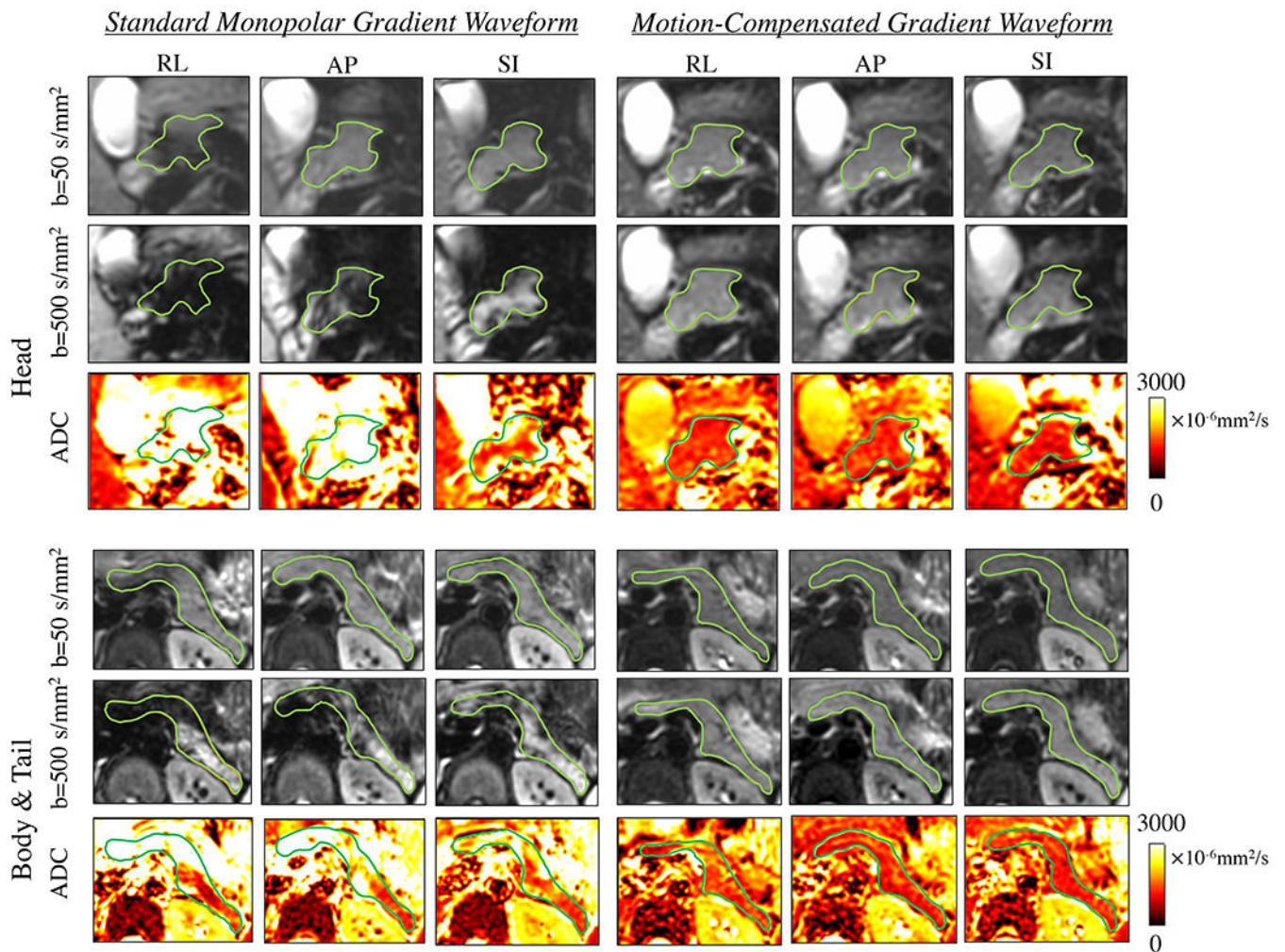
Figure 3.

Single-slice breath-hold diffusion-weighted images with b = 50, 500 s/mm^2 and ADC maps in three diffusion directions, at cardiac (peripheral-gating) trigger delay = 20 ms. The orange contours were drawn from DWI b = 50 s/mm^2 and overlaid on DWI b = 500 s/mm^2 and ADC maps to indicate pancreas location. Using a standard monopolar DW waveform, heterogeneous DW signals and ADC values were observed across the pancreas in all diffusion directions. Using a motion-compensated DW waveform, DW signals and ADC values appeared relatively uniform across the pancreas.

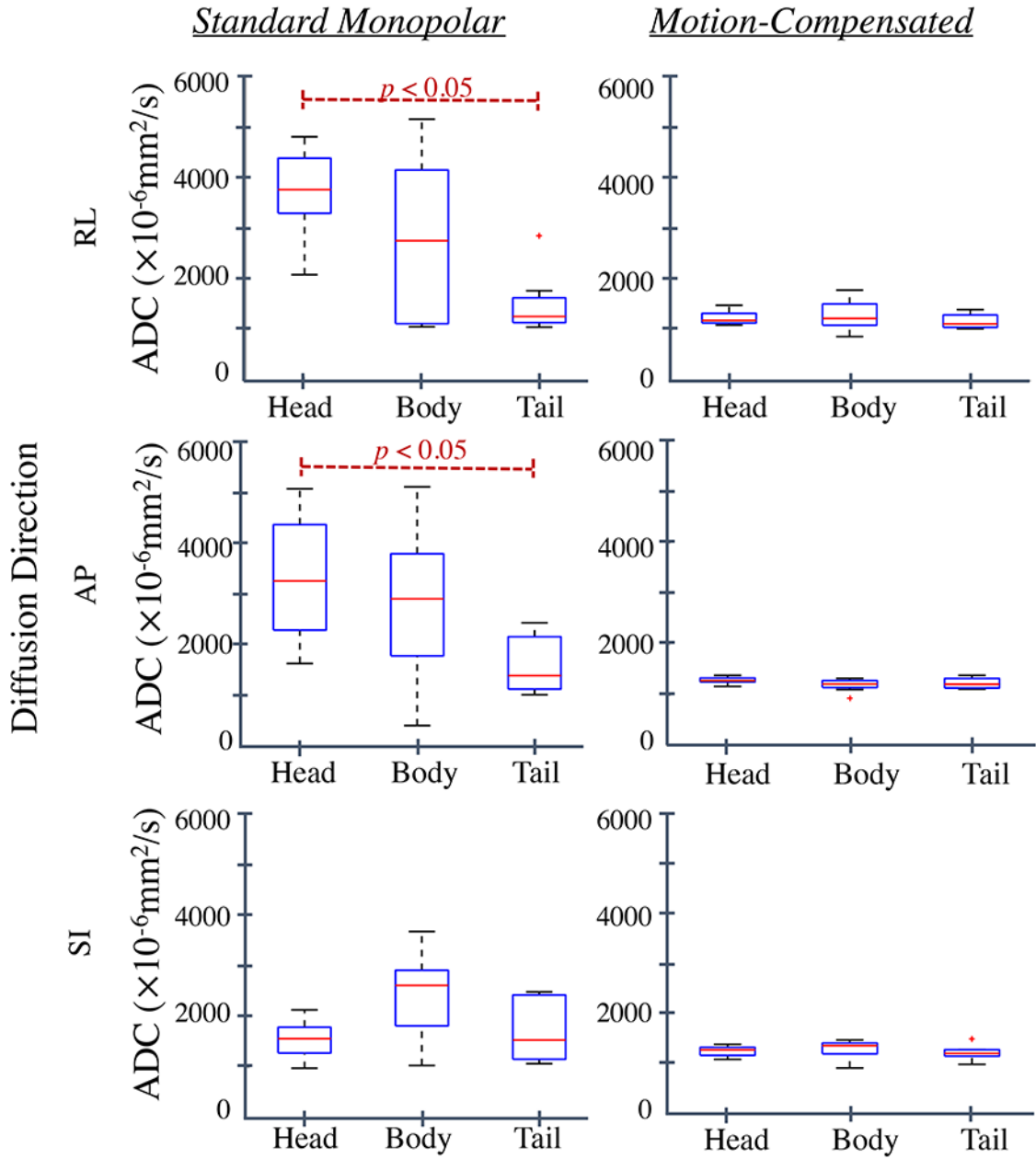**Figure 4.**

Boxplots of ADC measurements of eight volunteers derived from diffusion-weighted images acquired with $b = 50$ s/mm^2 and $b = 500$ s/mm^2 with standard monopolar and motion-compensated gradient waveforms in three diffusion directions in the breath-hold study. Using a standard monopolar gradient waveform, the measured ADCs had a large variability among volunteers and were higher in pancreas head and body than in the tail. Using a motion-compensated gradient waveform, the measured ADCs had a much lower variability among volunteers and were comparable across the parts of the pancreas.
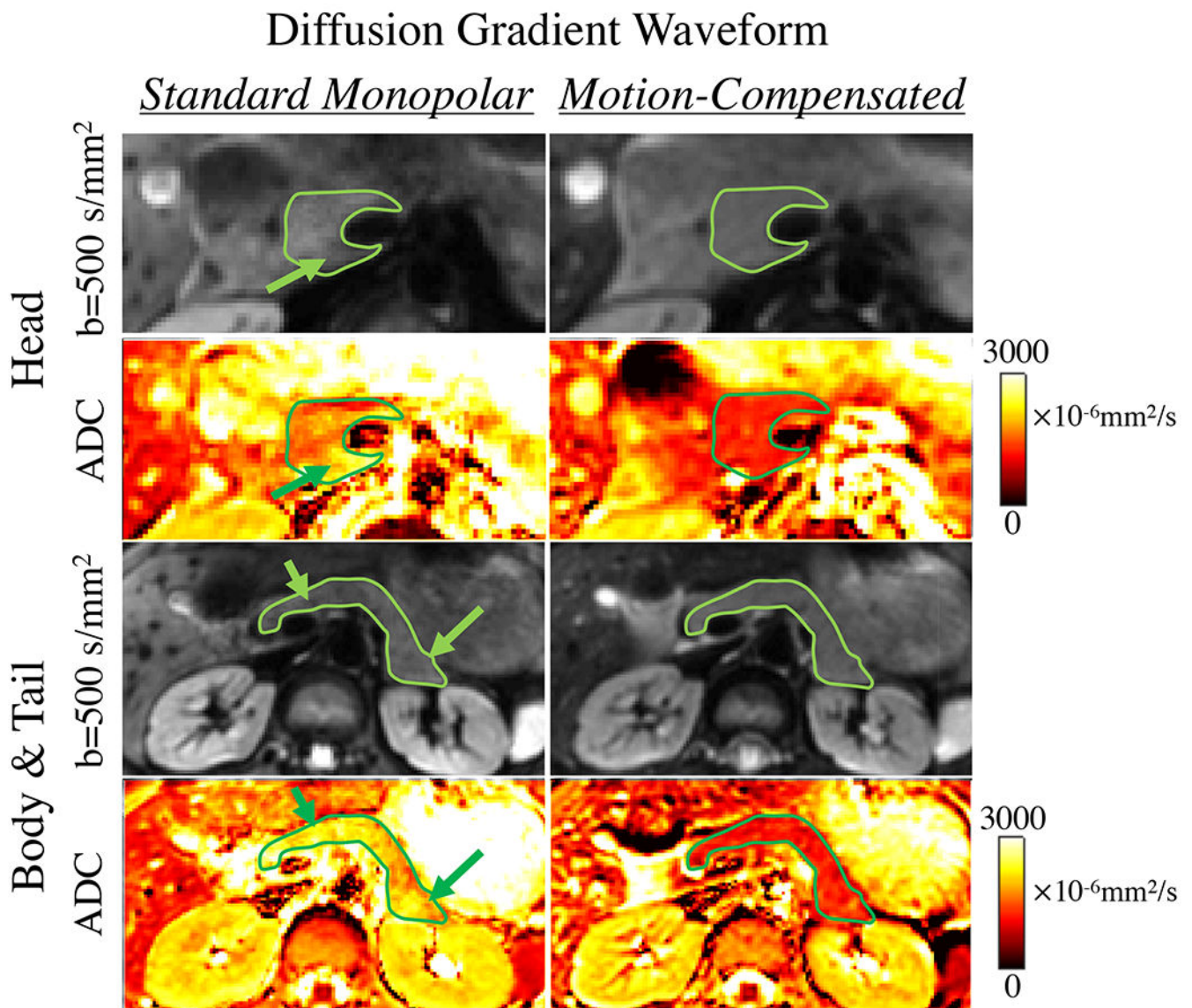
Figure 5.
Examples of DWI b = 500 s/mm^2 and ADC maps of the whole pancreas acquired with respiratory-triggering using standard monopolar and motion-compensated DW waveforms. Standard DW waveforms led to localized regions of signal dropouts, resulting in heterogeneous ADC values across the three parts of the pancreas. Green arrows indicate locations of artifactual signal dropouts. Since more repetitions and slices were acquired, the signal dropouts were blurred compared to the highly controlled single slice acquisitions shown earlier and the resulting elevated ADC values. Using a motion-compensated DW waveform, the measured ADCs were comparable across the parts of pancreas.
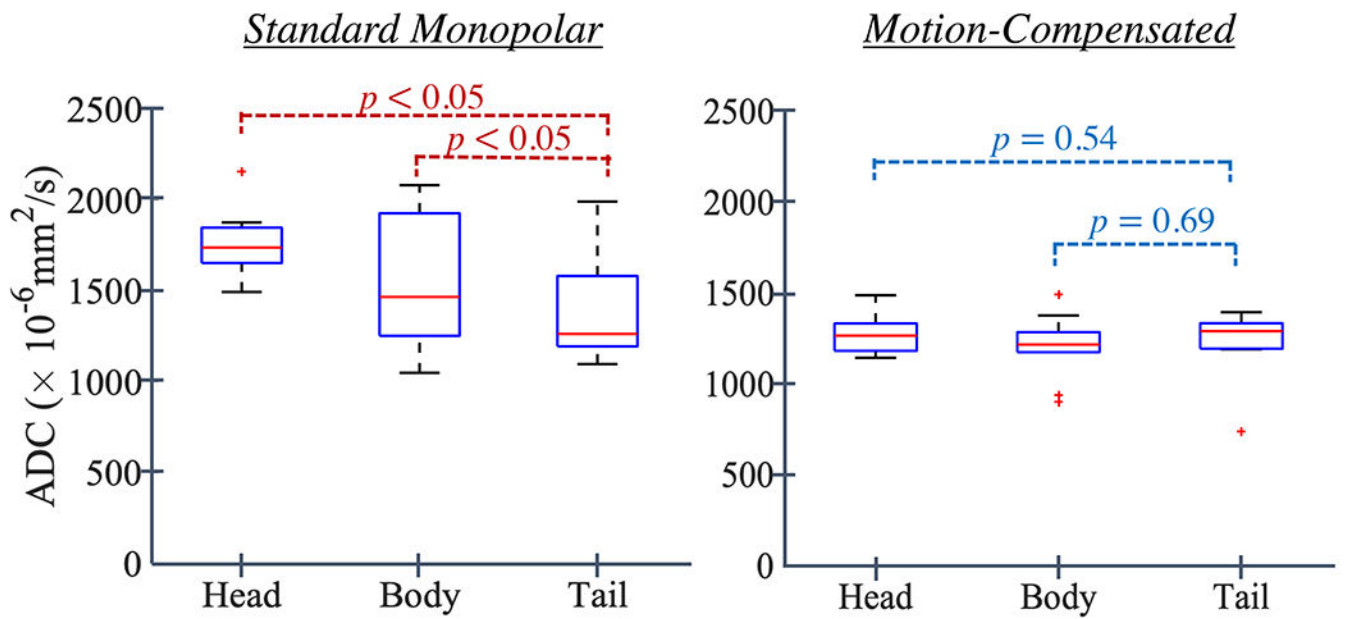
Figure 6.
Boxplots of ADC measurements of ten volunteers for the two waveforms in the respiratory-triggered study. Using a standard monopolar DW waveform, the measured ADCs in the pancreas head and body were significantly higher than in the tail. Using motion-compensated DW waveform, the measured ADCs had a lower variability among volunteers and were comparable in all three parts of pancreas.

Table 1.

Imaging parameters used for the in-vivo study. Single-slice DWI was acquired using breath-holding and cardiac (peripheral) gating. DW images were acquired in a single end-of-expiration breath-hold. This acquisition was repeated at three cardiac trigger delays (20, 100, and 200 ms), and in three diffusion directions using a standard monopolar waveform (TE = 50 ms). Reduced field-of-view (FOV = 40%) was used with spatial resolution = 2mm×2mm×5mm. Single-slice DWI using a motion-compensated gradient waveform (TE = 72 ms) was tested using the same parameters as standard monopolar waveform with trigger delay = 20 ms. Whole-pancreas DWI was acquired using respiratory-triggering with parameters similar to our local clinical protocol, including three diffusion directions. Two separate acquisitions were performed, using standard monopolar and motion-compensated gradient waveforms, respectively.

	Single-slice DWI		Whole-pancreas DWI	
DWI gradient waveforms	**Standard monopolar waveform**	**Optimized motion-compensated waveform**	**Standard monopolar waveform**	**Optimized motion-compensated waveform**
Acquisition modes	BH		RT	
TR (ms)	2069	1935	5000-10000 [*]	
TE (ms)	41.2	72.7	48.7	72.7
Cardiac Trigger Delays (ms)	20, 100, 200	20	--	
b-values (s/mm^2) (repetitions per direction)	0 (1), 50 (2), 500 (6)	50 (2), 500 (6)	50 (2), 500 (6)	
Reduced Field of view	40% in phase	100%		
Field of view	32 cm × 12.8 cm	32 cm × 32 cm		
EPI echo train length	48	60		
Effective phase encoding bandwidth	31 Hz	25 Hz		
Parallel imaging factor	1	2		
Diffusion directions	Phase, frequency, and slice (AP, RL, SI)			
In-plane resolution	2 mm × 2 mm			
Slice thickness	5 mm			
Slice spacing	1 mm			
Receiver bandwidth	± 250 kHz			
Partial Fourier	75%			

[*] 1-2 respiratory intervals depending on the breathing pattern of the volunteer.